CrossMark

TECHNICAL PAPER

A two-way FSI analysis of multiphase flow in hydrodynamic journal bearing with cavitation

D. Y. Dhande[1] · **D. W. Pande**[2]

Abstract This work deals with a study of a three-dimensional CFD analysis and multi-phase flow phenomena for hydrodynamic journal bearing with integrated cavitation. The simulations are carried out considering the realistic bearing deformations by two-way fluid–structure interactions (FSI) along with cavitation using ANSYS®Workbench software. The design optimization module is used to generate the optimized solution of the attitude angle and eccentricity for the combination of operating speed and load. Bearings with and without cavitation are investigated. A drop in maximum pressure value is observed when cavitation is considered in the bearing. The rise in oil vapor distribution is noted with an increase in shaft speed which lowers the magnitude of the pressure build up in the bearing. The bearing deformations are analyzed numerically and found increasing with an increase in shaft speed. The experimental data obtained for pressure distribution showed good agreement with numerical data along with a considerable reduction in computation time.

Abbreviations

e	Eccentricity between shaft and bearing, m
C	Radial clearance, m
R	Radius of the shaft, m
h	Film thickness, m
ω	Angular velocity, rad/sec
W	Load carrying capacity, N
O'	Bearing centre
O	Shaft centre
ρ	Fluid density, kg/m^3
ρ_l	Liquid density, kg/m^3
ρ_v	Vapor density, (kg/m^3)
$\vec{v}$	Fluid velocity
P	Static pressure, Pa
$\overline{\overline{\tau}}$	Stress tensor
$\vec{F}$	External body force, N
t	Time
ε	Eccentricity ratio
σ	Liquid surface tension coefficient
$\vec{v}$	Fluid velocity vector
C_e, C_c	Mass transfer source terms connected to the growth and collapse of the vapor bubbles, respectively
F_{cond}	Condensation coefficient
F_{evap}	Evaporation coefficient
p_v	Saturation pressure of the fluid
$[M_s]$	Structural mass matrix
$[M_f]$	Fluid mass matrix
$[F_s]$	Structural force matrix
$[F_f]$	Fluid force matrix
$[R]$	Coupling matrix
Δh	Relative rigid displacement of the two bearing surfaces
δ	Total elastic deformation of the shaft and bearing system

✉ D. Y. Dhande
dydhande@aissmscoe.com

D. W. Pande
dwp.mech@coep.ac.in

1 Department of Mechanical Engineering, AISSMS College of Engineering, Pune, Maharashtra 411001, India

2 Department of Mechanical Engineering, College of Engineering, Pune, Maharashtra 411005, India

$\underline{p}_b$	Bubble surface pressure
$\overline{\overline{I}}$	Unit tensor
μ	Fluid viscosity, Pa-s
R_b	Bubble radius, m
a_{nue}	Nucleation site volume fraction
p	Local pressure
θ	Angular coordinate
ϕ	Attitude angle
L	Length of the bearing

1 Introduction

The traditional method for hydrodynamic journal bearing analysis usually applies the lubrication theory based on classical Reynolds equation (Brizmer et al. [1], Buscaglia et al. [2], D'Agostino and Senatore [3]) which is simplified form of Navier-Stokes equations (Arghir et al. [4], Sahlin et al. [5], Li et al. [6]. and Wodtke et al. [7]) and continuity equation with usual thin film assumptions and thus has limitations in its applications. The solution of Reynolds equation is obtained using finite difference or finite element methods which lead to the subsequent development of simulation codes that integrate various numerical and empirical models taking into account physical phenomena such as turbulence, heat transfer, and cavitation. Even though these codes give reasonable results, however, they are limited for inability to visualize the physical phenomena in complex bearing models. These limitations could be circumvented by applying a computational fluid dynamics (CFD) approach coupled with FSI resting closer to the fundamental physical laws. Due to new rapid developments in computer software and hardware, it is possible to solve complex equations and many studies have been conducted using computational fluid dynamics (CFD) to solve lubrication problems that use the full Navier-Stokes equations to predict fluid flow applicable to complex phenomena.

Nassab [9] used CFD models to investigate pressures and temperatures in a plain journal bearing under laminar flow. Guo et al. [10] compared stiffness and damping properties using a CFD model with those from conventional Reynolds solutions for a plain journal bearing under laminar flow. Chen and Hahn [11] investigated inertia effects under laminar flow conditions in journal bearings and squeeze film dampers using CFD models. Tucker and Keogh [12] used a CFD model to analyze a journal bearing operating in the laminar regime including thermal and cavitation effects. Comparisons of their CFD results with experimental data for the same bearing geometry showed good agreement. Gertzos et al. [13] used CFD to model a bearing having an electro-rheological (Bingham) lubricant operating in the laminar regime. They showed good concurrence with experimental and analytical data from

previous investigations on Bingham fluids. Manshoor et al. [14] performed a CFD analysis of an oil-lubricated journal bearing using three different turbulence models. Their results showed good agreement among the three turbulence models, but did not list the range of Reynolds numbers analyzed. Ravikovich et al. [15] also performed CFD analyses of an oil-lubricated bearing, incorporating a fluid structure interaction (FSI) technique to match CFD film pressures with applied journal loads in bearings lubricated by oil, water, and gas. Their results for the oil bearing compared closely with those of a Reynolds model and an analytical solution, but no such comparisons were made for the water bearing. Dhande et al. [16] developed a CFD model along with FSI to calculate pressures in a laminar oil film including the effects of surface deformation. Their results showed significant pressure-induced surface deformation, especially at high journal eccentricities. Liu et al. [17] also used CFD with FSI to capture surface deformation effects. They developed a coupled CFD-FSI solution to solve the hydrodynamic pressures and bearing surface deformation simultaneously for improved solution efficiency. Using the coupled model, they analyzed an isoviscous, laminar, plain bearing having surface materials of varying elastic moduli supporting a rigid rotor which could be loaded either statically or dynamically. Their results found in line with a conventional Reynolds model and with experimental data for rigid bearing surfaces, and significantly higher journal eccentricities and rotor whirl amplitudes when the bearing surfaces were compliant. Qiyin Lin et al. [18] analyzed high-speed hybrid journal bearing using a combined approach of FSI and improved orthogonal experiment method for optimum design of recess parameters. The effect of design variables on friction force was studied and a significant decrease in friction force was observed. Recently Lihua Lu et al. [19]. presented a novel method based on fluid–structure interaction for optimal design of an aerostatic spindle which deals with the optimization of structural bearing parameters like supply pressure, diameter orifice and a number of the orifice.

It is concluded from the literature that the approaches used for solving journal bearing are based on either one of the following: (1) 2D analysis with cavitation approximation and constant viscosity neglecting viscous heating and (2) approximation of the thermal interaction of the films with solid components such as a shaft or bearing neglecting elastic deformation in components.

These approaches fail to give accurate performance resulting in an inability to visualize the realistic flow inside the bearings with complex geometries. Also, the said approaches use steady-state simulations with free floating shaft and transient simulation of CFD and structural analysis. The first approach lacks in dealing any imbalance in the shaft, thereby leading to contact between shaft and bearing

and hence perfect force balance is not accomplished. The second approach deals with long simulation time to reach an equilibrium position. The transient structural coupled with steady-state CFD approach works, but is complex and requires artificial damping to stabilize the structural motion. As the speed increases, bearing deformations increase resulting in modification of the fluid film flow regime in the bearing. Hence, dynamic remodeling of the geometry is necessary. Also, with the increase in speed, a fraction of oil will vaporize making the flow two-phase and the distribution of the vapor is wide that leads to a lower pressure build-up in a plain journal bearing with cavitation in comparison to a plain journal bearing without cavitation. This result differs from the Reynolds boundary condition solution to determine the onset of cavitation resulting in an increased pressure build-up. Wodtke et al. [7] and Lin et al. [8] worked on the analysis of bearings with cavitation coupled with FSI and found that the deformations are significant. Also, the cavitation problem becomes more severe with an increase in speed and significant computation time is required as observed by Geller et al. [20], Riedel et al. [21], Osman [22] and Montazeri [23]. Therefore, a need arises to develop a platform to compute the performance with cavitation, as well as bearing deformation caused by hydrodynamic forces that will lower the computational time and will give the optimum position of the shaft for the given combination of speed and load.

The aim of the present work is to study bearing pressure distribution by CFD-FSI methodology with the help of which the EHD performance can be accurately predicted. The phase change process is also modeled to consider cavitation in bearing. The mixture model is used to account for cavitation and parametric modeling is employed to modify the flow domain as the bearing deforms. The CFD and FSI modules are system coupled and design optimization module is applied to get the optimum position of the shaft.

2 Geometry description

The journal bearing geometry used in the present work is shown in Fig. 1. The bearing center is represented by O' and O is the journal or shaft center, 'e' is the eccentricity between the shaft and bearing centers and 'L' is the bearing length. The external load 'W' is assumed as acting vertically along the Y-axis and is constant.
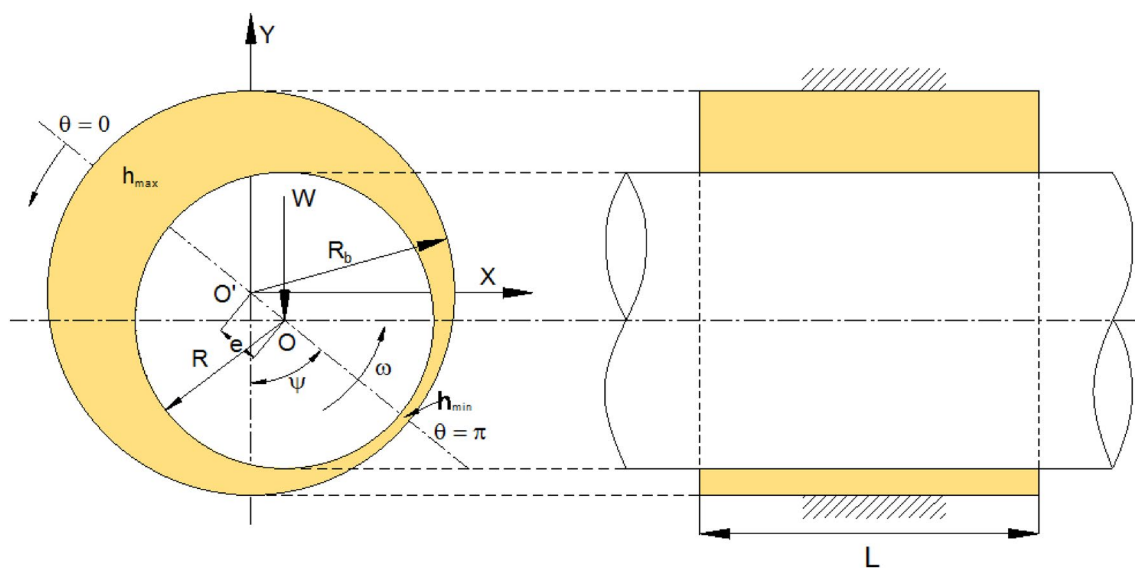
3 Theory

3.1 Governing equations

The pressure distribution in the hydrodynamic journal bearing is obtained by solving Navier-Stokes continuity and momentum equations. In FLUENT, these equations are solved for mass and momentum which are valid for all types of flows. The general mass conservation equation for compressible as well as the incompressible flow is given as:

$$\frac{\partial \rho}{\partial t} + \nabla \cdot (\rho \vec{v}) = 0 \tag{1}$$

where, ρ and $\vec{v}$ are the fluid density and fluid velocity vector, respectively.

The momentum equation is:

Fig. 1 Hydrodynamic journal bearing geometry

3402

J Braz. Soc. Mech. Sci. Eng. (2017) 39:3399–3412

$$\frac{\partial}{\partial t} (\rho \vec{v}) + \nabla \cdot (\rho \vec{v} \vec{v}) = -\nabla P + \nabla \cdot (\overline{\overline{\tau}}) + \rho \vec{g} + \vec{F} \tag{2}$$

where, P is the static pressure, $\overline{\overline{\tau}}$ is the stress tensor (given in Eq. 3 below), $\rho \vec{g}$ is the gravitational force and $\vec{F}$ is the external body force.

The stress tensor is written as,

$$\overline{\overline{\tau}} = \mu \left[\left(\nabla \vec{v} + (\nabla \vec{v})^T \right) - \frac{2}{3} \nabla \cdot \vec{v} \overline{\overline{I}} \right] \tag{3}$$

where, μ is fluid viscosity, $\overline{\overline{I}}$ is the unit tensor, and the second term on the right-hand side is the effect of volume dilation.

3.2 Cavitation

The eccentricity between shaft and bearing creates a convergent–divergent wedge. In the convergent region, pressure increases due to wedge effect. The fluid properties will remain constant as long as the only liquid is present in this area. When the fluid enters the divergent zone, the pressure falls and reaches the saturation pressure at a given temperature. At this stage, the gas dissolved in the fluid is released in the form of bubbles, flowing as a free gas. As the fluid advances further in the divergent region, the free gas expands and new releases from the liquid take place. This flow is assumed as isothermal, as the amount of gas released is usually small, so that the energy required for the phase change can be neglected. As the flow once again advances to the convergent region of the bearing, the upstream higher pressures react with fluid by diffusion of momentum. The pressure recovery takes place before recirculating through the convergent region. Again the pressure increases and gas is redissolved in the oil. However, the absorption rate is much slower than release, the liquid may not be able to absorb the gas completely in the flow time available in a positive pressure region. This phenomenon involving the release of dissolved gas at pressures below saturation pressure, growing of gas bubbles and redissolving into a liquid at higher pressures is termed as cavitation. This process is illustrated in Fig. 2.

There are two types of cavitation which occur in the journal bearing. When the pressure drops below the equilibrium pressure, parts of the dissolved gasses are set free. This is called as gaseous cavitation. If the pressure drops further below the vapor pressure, the oil starts to evaporate, which is termed as vapor cavitation [20, 24].

In cavitation, the oil–vapour mass transfer is governed by the vapor transport equation given below

$$\frac{\partial}{\partial t} (a_v \cdot \rho_v) + \nabla (a_v \cdot \rho_v \cdot v_v) = C_e - C_C \tag{4}$$
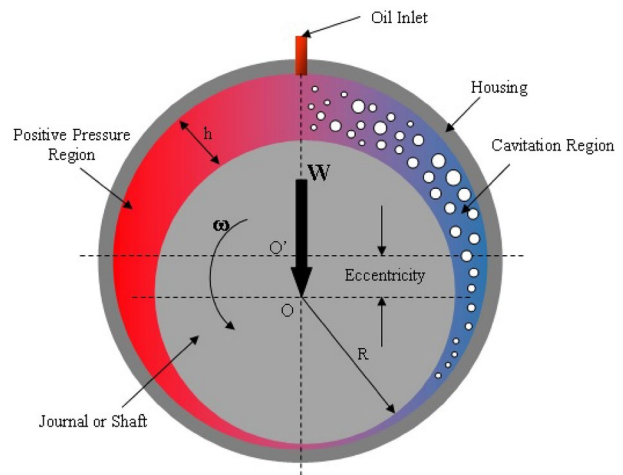
Fig. 2 Cavitation process and release of the dissolved gas in the liquid

where C_e and C_c account for the mass transfer between the liquid and vapor phases in cavitation. They are based on the Rayleigh–Plesset equation which provides a good approximation of vapor cavitation. The growth of a single vapor bubble in a liquid is governed by the following equation:

$$R_b \cdot \frac{d^2 R_b}{dt^2} + \frac{3}{2} \left(\frac{dR_b}{dt} \right)^2 = \frac{p_b - p}{\rho_l} - \frac{2\sigma}{\rho_l \cdot R_b} - 4 \cdot \frac{\mu_l}{\rho_l \cdot R_b} \cdot \frac{dR_b}{dt} \tag{5}$$

Neglecting the second order terms and the surface tension force, Eq. (5) is simplified to:

$$\frac{dR_b}{dt} = \sqrt{\frac{2}{3} \cdot \frac{p_b - p}{\rho_l}} \tag{6}$$

This equation provides a physical approach to introduce the effects of bubble dynamics in the cavitation model. It can also be considered an equation for void propagation and hence mixture density. In the present work, Zwart-Gerber-Balamri model [25] is used, which assumes that all the bubbles in a system have the same size. The final form of this cavitation model is as follows:

If, $p < p_v$

$$C_e = F_{evap} \cdot \frac{3 \cdot a_{nue}(1 - a_v) \cdot \rho_v}{R_b} \cdot \sqrt{\frac{2}{3} \cdot \frac{p_v - p}{\rho_l}} \tag{7}$$

If $p \geq p_v$

$$C_C = F_{cond} \frac{3 \cdot a_v \cdot \rho_v}{R_b} \cdot \sqrt{\frac{2}{3} \cdot \frac{p - p_v}{\rho_l}} \tag{8}$$

R_b bubble radius $= 10^{-6}$ m, a_{nue} nucleation site volume fraction $= 5 \times 10^{-4}$, F_{evap} evaporation coefficient $= 50$, F_{cond} condensation coefficient $= 0.01$.

3.3 Fluid structure interaction (FSI)

The fluid structure interaction involves the coupling of fluid dynamics and structural mechanics modules. Fluid flow exerts a hydrodynamic force on the bearing causing it to deform thus modifying the flow domain. There are two modes of FSI modeling: One-way FSI and two-way FSI. In one-way FSI, the calculated flow, and thermal fields are passed from CFD to FEA codes and generally used for smaller deformations in structures and there is no need of updating and recalculation of flow.

In two-way FSI (Fig. 3), iteration between CFD and FEA code takes place and the flow is modified according to structural deformations. In this work, two-way FSI is used to find deformations in the bearing and the dynamic remodeling of the flow. The static structural capability of ANSYS is used to find deformations in the bearing and CFD is applied to calculate hydrodynamic pressure and forces. These two modules are system coupled to get a modified flow domain due to bearing deformations.

The governing equations are:

$$[M_s]\{\ddot{U}\} + [K_s] \cdot \{U\} = [F_s] + [R] \cdot \{P\} \tag{9}$$

$$\begin{bmatrix} M_s & 0 \\ \rho R^T & M_f \end{bmatrix} \cdot \begin{Bmatrix} \ddot{U} \\ \ddot{P} \end{Bmatrix} + \begin{bmatrix} K_s & R \\ 0 & K_f \end{bmatrix} \cdot \begin{Bmatrix} U \\ P \end{Bmatrix} = \frac{F_s}{F_f} \tag{10}$$

where $[M_s]$ is the structural mass matrix; $[M_f]$ is the fluid mass matrix; $[F_s]$ and $[F_f]$ is the structural and fluid force matrix; $[R]$ is a coupling matrix that represents the effective surface area associated with each node in the fluid–structure interface. The flow chart for two-way FSI solution technique is shown in Fig. 4 below.
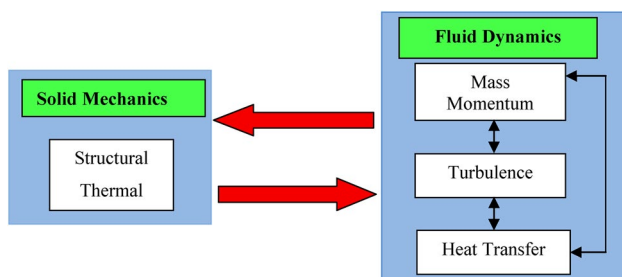
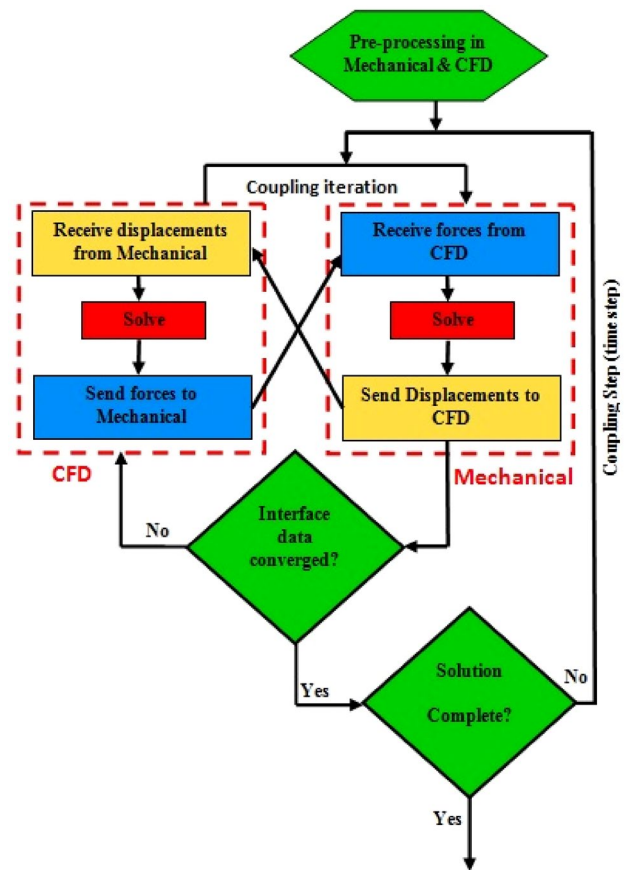**Fig. 3** Two-way fluid structure interaction

Fig. 4 Two-way FSI solution technique

3.4 Lubricant film thickness

The relative displacement of the fluid–structure interfaces in the fluid domain is consistent with that of the solid domain. The film thickness is the distance between the rotor–lubricant interface and the bearing–lubricant interface, including both rigid and elastic deformations between the two bearing surfaces and is defined as,

$$h = C + \Delta h + \delta \tag{11}$$

where h is the film thickness, C is the radial clearance of the bearing system, Δh is the relative rigid displacement of the two bearing surfaces and δ is the total elastic deformation of the two bearing surfaces.

3.5 Assumptions and boundary conditions

The Navier–Stokes equations are solved using 3D double precision pressure based steady-state analysis. As the Reynolds number is very low, laminar and isothermal flow conditions are assumed. The fluid domain, shown in

3404

J Braz. Soc. Mech. Sci. Eng. (2017) 39:3399–3412

Fig. 5 Three-dimensional finite element representation of journal bearing system. **a** Geometry and mesh details of fluid domain: oil film. **b** Geometry and mesh of solid domain: journal and bearing
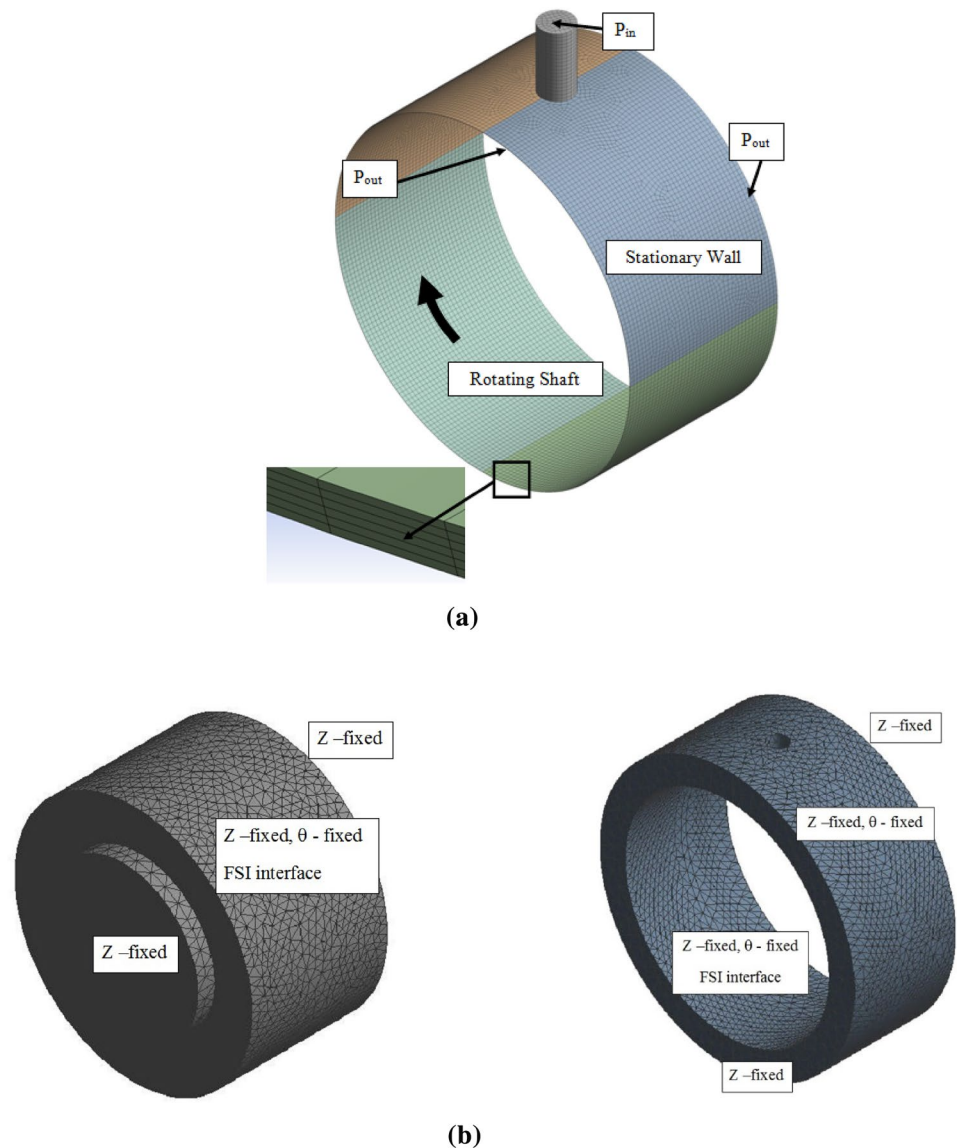
Fig. 5a is meshed using hexahedral elements in CFD. The lubricant film is provided with 6 layers in the radial direction. Element size of 0.5 mm is used to give a total number of elements 102636. The solid domain, shaft and bearing, shown in Fig. 5b is meshed using tetrahedral meshing with 184145 elements. The lubricant supply hole is defined as 'pressure inlet' and the sides of the lubricant are specified as 'pressure outlet' with a gauge pressure as a zero. The inlet pressure is taken as 101.325 kPa. The bearing is modeled as 'stationary wall' and the shaft is modeled as 'moving wall' with absolute rotation speed. Initially, the shaft axis position is defined by an arbitrary value of eccentricity and the attitude angle, and these values are fed as input to shaft rotation axis origin. To model the change in thickness of fluid domain, the dynamic mesh technique [26] is used. The mesh is then transferred to FLUENT for flow analysis. The smoothing mesh method is used with a convergence tolerance of 10E−6 and the number of iterations are 50.

3.6 Design explorer approach

The method is based on finding out the equilibrium position of the shaft where there is a force balance between the shaft load and fluid reaction forces at a constant speed and shaft load. At equilibrium position, the fluid forces in the vertical direction (X-load) balance the shaft load (*W*) and the fluid forces in the horizontal direction (Y-imbalance) are zero. Initially, for given load and speed, the shaft rotation axis is fixed at a predefined position in terms of eccentricity and attitude angle in parametric form and the system is solved

to get fluid forces in X and Y direction. The fluid forces are computed in computational fluid dynamics (CFD) domain and structural deformations are computed in structural domain. These two systems are system coupled to perform elastohydrodynamics. The fluid forces developed in CFD are transferred to the structural domain and vice versa. Then design optimization is carried out to find the equilibrium position of the shaft. Initially, since the shaft rotation axis is fixed, i.e.as it is not allowed to float, perfect balance in X and Y direction is not achieved. Hence design exploration cannot be used to get a response surface with different shaft positions and equilibrium position. Figure 6 presents details of response surface showing shaft positions in terms of eccentricity versus X-direction fluid reaction force while Fig. 7 shows the shaft position versus Y direction fluid reaction force. The objective is to find a point on this response surface where Y-imbalance is zero and fluid reaction force in X-direction balances the shaft load. So the problem is transformed into optimization with the targets to seek the Y-imbalance zero and X-load equal to shaft load giving the correct equilibrium position of the shaft.

The design exploration has three stages viz. the design of experiments (DOE), response surface analysis (RSA) and optimization. DOE is used to determine a set of eccentricities and attitude angles that are used to build response surface. The values for upper and lower bound of the eccentricity and attitude angle are specified within which the solution is expected. An optimal space filling design algorithm is used to get design points and a matrix of experiments is generated. These design points are used to build response surface which analyses the relationship between eccentricity, attitude angle and output parameters (fluid reaction forces).

The goodness of fit shown in Fig. 8 is observed to see how well the surface fits close to the data points. The response surfaces are examined to find the values of potential solutions which satisfy the optimization criteria. The optimization is based on response surface evaluation. Multi-objective genetic algorithm.

(MOGA), which is based on controlled elitism concepts with non-parametric regression analysis is used. It supports multiple objectives and constraints to find the globally optimal solution. To get the more close solution, more refinement design points are added to the solution and the process is repeated till the optimum equilibrium position of the shaft is achieved.

The dimensions and the properties of the materials used in this study are listed in Table 1.
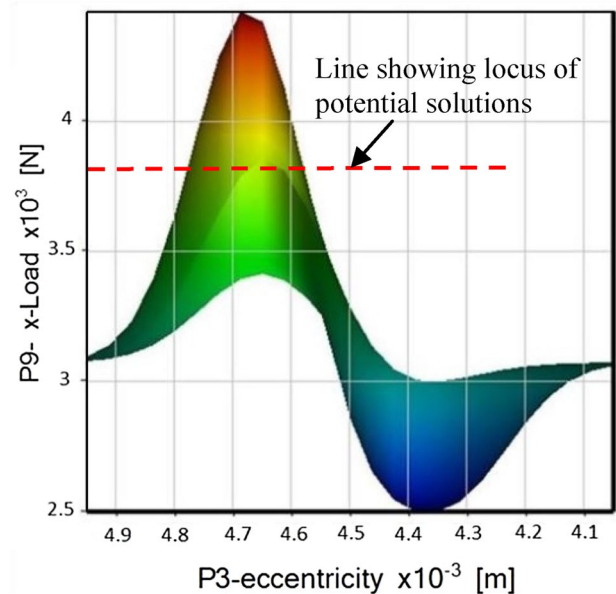

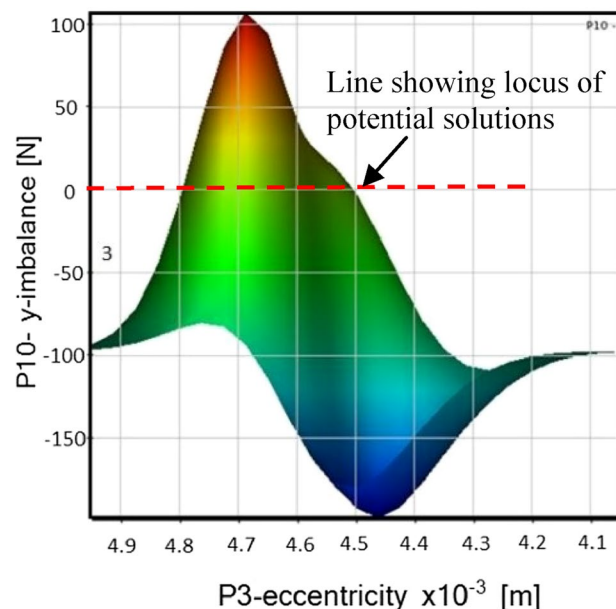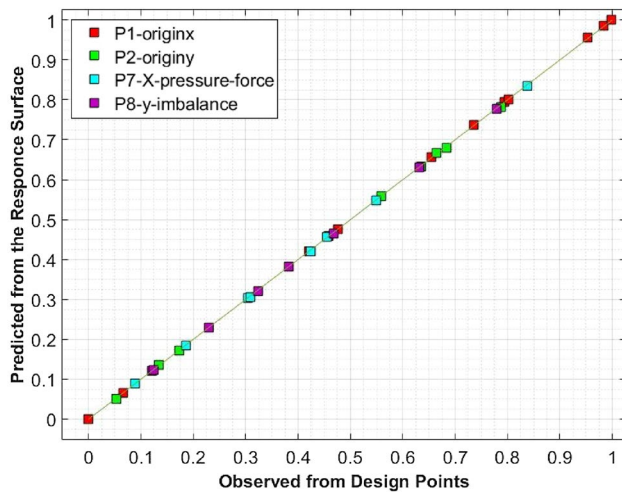**Fig. 6** Response surface for vertical load

Fig. 7 Response surface of horizontal (X) imbalance

4 Experimental setup

The experimental setup consists of a shaft of 50 mm diameter supported in two self-aligned bearings and the test bearing floats on the shaft as shown in Fig. 9b. The shaft made up of structural steel is driven with the help of a 3 phase

Fig. 8 Goodness of fit curve

Table 1 Parameters used in the analysis

Parameter	Value
Shaft diameter, D	0.05 m
Clearance, C	5×10^{-5} m
Length of the bearing, L	0.025 m
Speed, N	1000, 2000, 3000, 4000, 5000 RPM
Lubricant viscosity, μ	0.0125 Pa-s
Lubricant density, ρ	850 kg/m^3
Oil vapor saturation pressure	29,185 Pa
Oil vapor dynamic viscosity	2×10^{-5} Pa-s
Material	
Shaft: structural steel	Elastic modulus = 200 GPa
	Density, $\rho_s = 7850$ kg/m^3
	Poison ratio = 0.3
Bearing: aluminium	Elastic modulus = 210 GPa
	Density, $\rho_A = 2700$ kg-m^3
	Poison ratio = 0.334

5 HP drive motor with a rated speed of 1440 RPM and its speed is controlled with the help of variable frequency drive whose frequency can be varied in the range of 0–100 Hz. A pulley setup is designed to step up the speed of the motor from its rated speed. The bearing is loaded with the aid of a flat belt and the loading is sensed with S type strain gauge load cell of capacity 1000 N (±100 g). There are nine pressure sensors (M5100 $\pm$ 0.25% FS) mounted at the mid-plane of the bearing circumferentially at an angle of 18° from the horizontal plane in the loaded zone as shown in Fig. 9a to measure circumferential pressures.

Digital indicator is used to display the pressure readings and the location can be changed using multipoint indicator switch. The eccentricity is measured with

the help of inductive type proximity sensor (IWRM 06U9501), with a resolution of 0.1 microns and accuracy 1–3%, mounted on bearing housing and connected to a data acquisition system (8 Channel with inbuilt A/D converter) for recording. The test oil used is supplied through an inlet supply system consisting of gear pump at a constant pressure. The test bearing is shown in Fig. 9c.

The tests are carried out at a speed ranging from 1000 to 5000 RPM. The loading is provided with the help of belt arrangement. The desired speed is set with the help of variable frequency drive. The system is allowed to achieve a steady-state for half an hour and corresponding pressures and eccentricities are measured. Three sets of the readings were taken at each speed and the average reading is taken for the analysis. The experimental results are plotted and compared with the numerical results.

5 Results and discussion

5.1 Grid independence study

In the numerical simulation of the hydrodynamic journal bearing, the mesh independence study was conducted at eccentricity ratio 0.8 and rotation speed 3000 RPM to ensure the accuracy of the solution. Mesh density was checked in three directions for fluid domain: axially, circumferentially and radially and the obtained maximum pressure values were compared. The grid independence was satisfied at 102636 cells in which the number of divisions in axial, circumferential and radial direction are 50,360, 6, respectively. The obtained results shown in Table 2, reflect no significant influence on the results. A similar study of the sensitivity of mesh density on solid domain revealed an even smaller influence.

5.2 Validation study

The numerical case was developed using proposed approach and the numerical results in published data represented in references by Guo et al. [10] were compared. The lubricant supply pressure was 101,325 Pa, the rotational speed of 10,000 RPM and 25 micron film thickness was assumed. The value of attitude angle and load carrying capacity is predicted neglecting elastohydrodynamic as well as cavitation effects. The proposed numerical method gives a value of attitude angle 52.23°, load carrying capacity of 1160.38 N and maximum pressure 2.1523 MPa at an eccentricity of 25.19 microns as compared to 49.8°, 1160 N and 2.31 MPa at 25 microns eccentricity given by Guo et al. This is acceptable since cavitation, as well as elastohydrodynamic effect, reduce the maximum pressure developed in the convergent region. This validates the proposed numerical method.

Fig. 9 a Pressure sensor
arrangement; **b** test setup; and **c**
test bearing
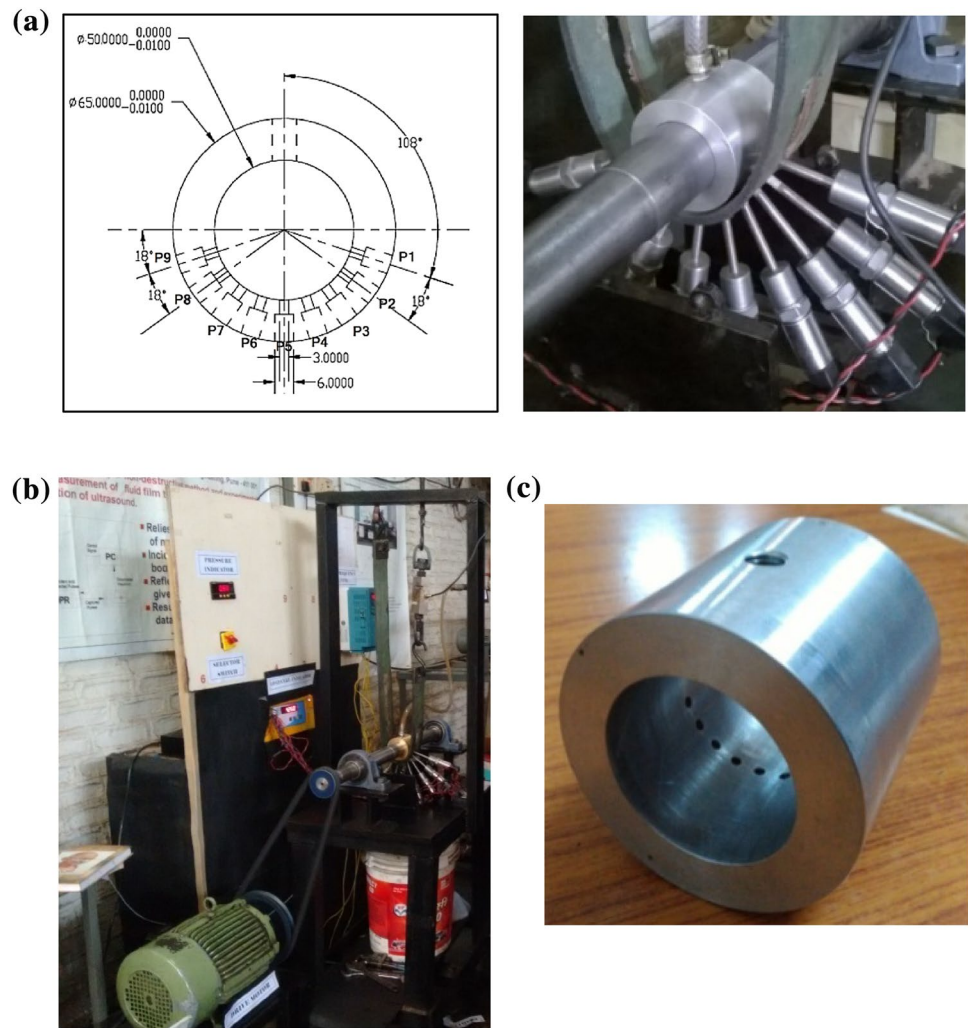
Table 2 FSI analysis results for fluid domain for various mesh grid densities

Direction			P_{max} (MPa)	Bearing deformation (δ_{max}), (μm)
Circumferential	Axial	Radial		
360	40	4	5.528	0.48391
360	50	4	5.594	0.48795
360	60	4	5.546	0.48505
360	80	4	5.520	0.4820
360	40	6	5.886	0.50403
360	50	6	5.890	0.51552
360	60	6	5.901	0.51652
360	40	10	5.898	0.51843
360	50	10	5.912	0.51751

5.3 Effect of cavitation

The numerical results are given for the journal bearing when the journal bearing is loaded and the shaft is eccentric to the bearing position which generates a positive pressure to support an external load applied. Figure 10a shows a pressure built up and pressure drop in a journal bearing and in Fig. 10b, the pressure distribution is changed to a pressure build up and the pressure drop has disappeared due to cavitation. The pressure build up lies closer to the smallest gap and ends behind the smallest gap that leads to a different reaction on the shaft. This corresponds to the Reynolds boundary condition which states that the gradient of the pressure over the angle should be zero.

The comparison of maximum pressure developed for bearing with and without cavitation is presented in Fig. 11 at various operating speeds. The magnitude of the pressure build up is also changed, which is slightly lower than the pressure build up without cavitation.
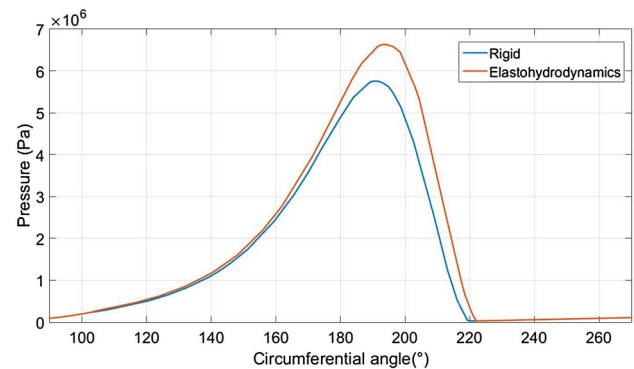
The comparison of the circumferential pressure distribution in the convergent zone is shown in Fig. 12 for both bearings, which indicates that the peak pressure in a journal bearing without cavitation is more than that of

3408

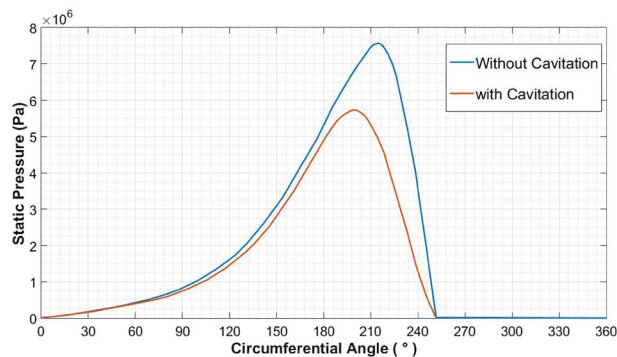J Braz. Soc. Mech. Sci. Eng. (2017) 39:3399–3412
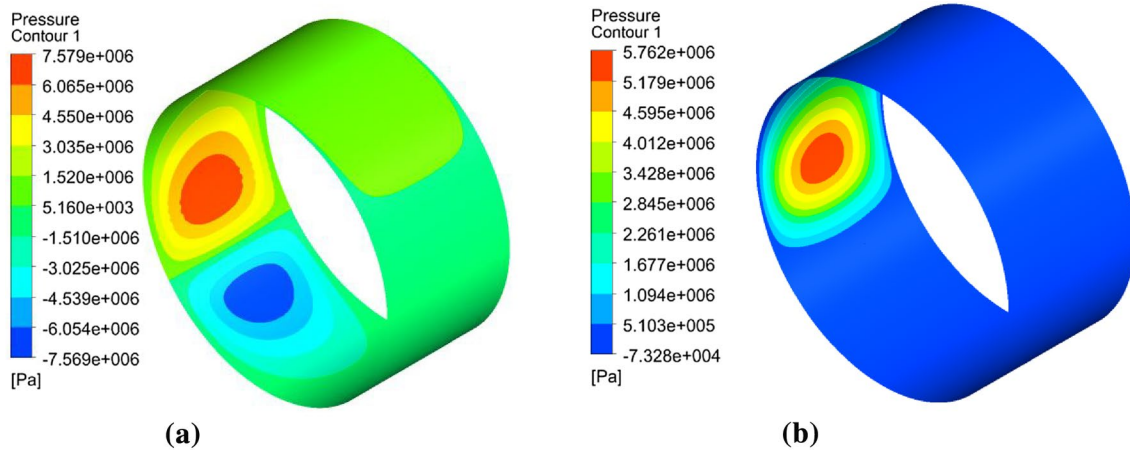
Fig. 10 Pressure contours generated in the journal bearing. **a** With cavitation. **b** Without cavitation
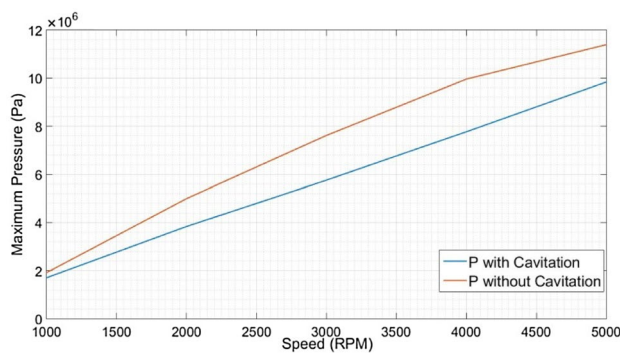
Fig. 11 Comparison of maximum pressures in journal bearing with and without cavitation

Fig. 13 Comparison of circumferential pressure distribution in journal bearing with rigid and elastohydrodynamic assumption


Fig. 12 Comparison of circumferential pressure distribution in a journal bearing with and without cavitation

with cavitation. This confirms the fact that the cavitation lowers the peak value of the positive pressure builds up.

Figure 13 shows the comparison between the numerical pressure distribution with rigid (Boyd and Raimondi assumption) and with elastohydrodynamic consideration.

It is evident that the peak pressure value drops when elastic deformations are considered as compared with the rigid maximum pressure value. Due to elastic deformation in the bearing, the clearance space between the shaft and bearing increases, which allows more lubricant to fill in the space reducing the maximum pressure generated as compared to rigid assumption.

The simulation of the bearing is carried out using two-way FSI. Figure 14a shows deformation of the bearing, Fig. 14b shows the pressure distribution of fluid without considering FSI and Fig. 14c shows pressure field distribution of fluid considering FSI. It can be seen that the maximum deformation of the bearing is 0.48391 μm, which causes redistribution of the flow field and change of static characteristics of the bearing. These deformations are very small at lower speeds and eccentricities, but go on increasing with increase in speed (as seen from Table 3) and make considerable modifications in the clearance space thus modifying the performance parameters. Hence, it is very much important to consider these deformations due to fluid
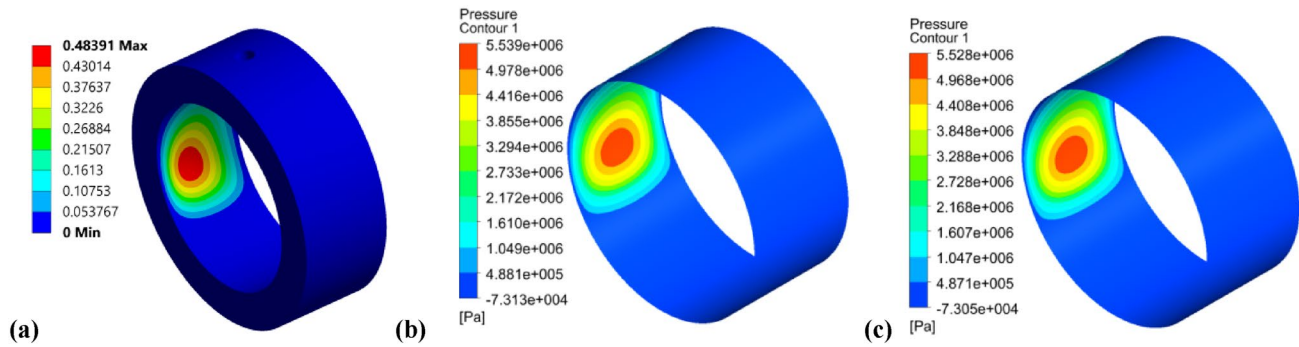
Fig. 14 Pressure distribution of the fluid and deformation of the bearing at various instances (**a**) deformation of the bearing, (**b**) the pressure distribution of the fluid without considering FSI and (**c**) the pressure distribution of the fluid considering FSI at 3000 RPM and eccentricity ratio 0.8

Table 3 Deformation and maximum pressure various speeds and $\varepsilon = 0.8$

| Speed (N) (RPM)	Max. pressure (P_{max}) (MPa)	Bearing deformation (δ_{max}), (μm)
1000	1.934	0.1612
2000	3.823	0.3225
3000	5.762	0.4831
4000	7.764	0.64781
5000	9.851	0.8106

force to predict the accurate performance of hydrodynamic journal bearings.

Table 2 lists the values of maximum pressure developed in the fluid film and corresponding maximum deformations in the bearing at various speeds and constant eccentricity ratio 0.8.

5.4 Effect of rotational speed and eccentricity ratio

Figure 15 shows the comparison between numerical results and experimental data for pressure distribution on the mid-plane of the shaft for various eccentricity ratios (ε). It is noted that the peak pressure goes on increasing with the increase in the eccentricity ratio (ε). The peaks are low for lower eccentricity ratio (ε) values, but are significant when eccentricity ratios (ε) are 0.8 and 0.9. Also, the range of peak pressure becomes narrow at these two values. When the eccentricity ratio (ε) is in the range of 0.2–0.6, the peak pressure value is too low to separate the journal and bearing.

Figure 16 shows the comparison between numerical results and experimental results of pressure distribution for eccentricity ratio (ε) 0.8 at various rotational speeds of the shaft. The peak pressure increases with increase in rotational speed of the shaft, but the range of peak pressure goes on gradually reducing as compared to the peak
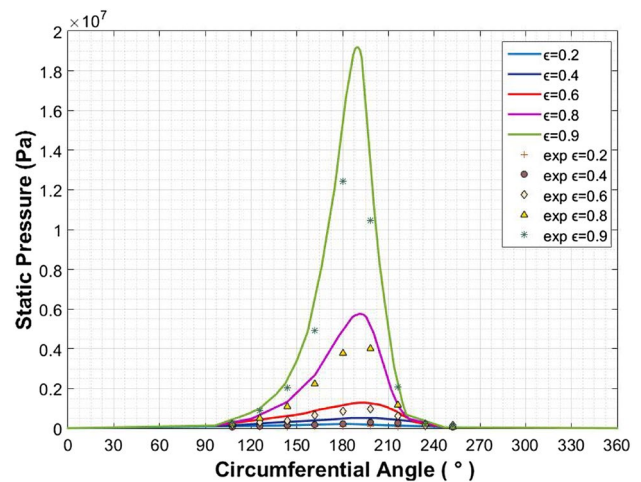
Fig. 15 Comparison of circumferential pressure distribution for CFD model and experimental data at various eccentricity ratios ($N = 3000$ RPM)
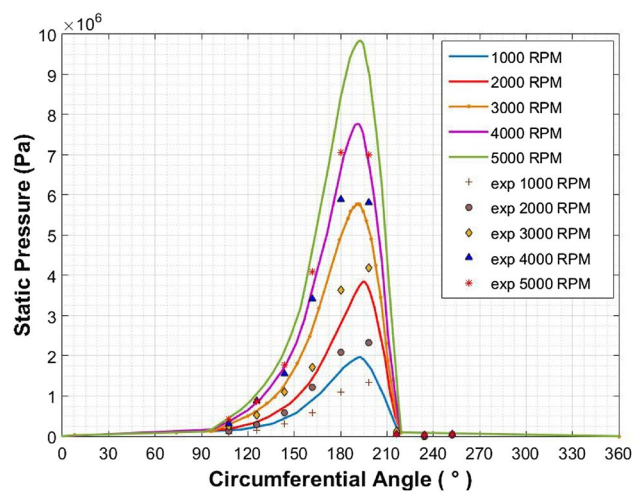
Fig. 16 Comparison of circumferential pressure distribution for CFD model and experimental data at various shaft speeds for $\varepsilon = 0.8$

3410

J Braz. Soc. Mech. Sci. Eng. (2017) 39:3399–3412

pressure range in the case of the eccentricity ratio (ε). Also for eccentricity ratio 0.8–0.9, there is a steep rise in peak pressure at constant speed ($N = 1000$ RPM) whereas, in the case of the constant eccentricity ratio ($\varepsilon = 0.8$), the pressure goes on increasing gradually.

5.5 Effect of rotational speed on vapor volume fraction

Figure 17 shows the effect of rotational speed on the vapor volume fraction in the oil film for eccentricity ratio 0.8. As the rotational speed increases from 1000 to 5000 RPM, the cavitation area and the vapor volume fraction increase in the divergent region due to drop in film pressure below the vapor pressure initiating oil evaporation. This is significant since it is assumed in theories that after the inlet, all the vapor bubbles are expelled. It can be explained by the high rotational speed of the shaft. The shaft drags vapor bubbles to the inlet tube, where the new liquid oil enters the journal bearing. This new liquid oil does not have the force to expel the vapor bubbles because it is also dragged by the fast rotating shaft. When the film is converging, the liquid oil is squeezed and pushes the vapor bubbles out of the journal bearing. It also explains the lower magnitude of the pressure build up, because the pressure build up will appear only in liquid oil. Therefore, the pressure build up cannot increase as much as in the journal bearing without cavitation. The remaining oil in the cavitation area is thrown against the housing of the journal bearing and the vapor bubbles stay closer to the shaft, which is caused due to the difference in density. The remaining oil in the convergent region is thrown out by the centrifugal force due to the speed of the shaft, which would suggest that velocity slip between the oil and the vapor bubbles appears in a journal bearing while the velocity slip is not considered in the cavitation model. The pressure build up is not sufficiently lower when velocity slip is considered in the cavitation model. The velocity slip between the oil and air bubbles is hence neglected for the simulations with cavitation.

The CFD-FSI approach is implemented to predict pressure distribution in hydrodynamic journal bearing. This approach coupled CFD with FSI, the elastic deformation and structural dynamics of the bearing and shaft, and the phase change in the fluid domain. The CFD-FSI interfaces are system coupled with design optimization in order to get the optimum position of the shaft. Each of these issues is listed in the literature, but the integration of CFD-FSI with the design optimization approach is novel and proves to be a powerful tool for the analysis of the fluid domain involving EHD situations.

From Figs. 10, 11 and 12, it is observed that the phase change in the fluid has a substantial effect on bearing performance. The peak pressure values drop due to cavitation when the phase change is considered. The drop in pressure

value increases with increase in rotational speed. This may be due to the acceleration of release of dissolved gas in the fluid at elevated rotational speeds, giving rise to increased amount of cavitation thereby lowering peak pressure values.

From the Figs. 13, 14 and Table 2, it is seen that the elastic deformation in the bearing has a great influence on the pressure distribution. The CFD-FSI coupled approach predicts oil film pressure and bearing deformations simultaneously, thus providing a useful tool for bearing design.

The largest computation time required for the CFD-FSI interaction in the study is 180 min for simulating a bearing with mesh $360 \times 100 \times 10$ with a total number of cells 624459 using Intel (R) Core (TM), i5-3210 M CPU@2.50 GHz,8 GB RAM, personal computer. This time is acceptable as compared to traditional user developed codes as CFD-FSI approach has potential to consider many parameters which cannot be included in another approach and the time required to modify the codes is much more and more complex in traditional approaches.

6 Conclusions

The work studied deals with hydrodynamic journal bearing analysis with the multiphase flow. A new numerical method comprising of CFD and FSI methodology with optimization has been implemented. Both inertial, as well as cavitation effects, are considered. The experimental data obtained provides very good concordance with numerical results. The following conclusions can be made regarding the results obtained:

1. The magnitude of the pressure build up lowers as compared to the pressure build up in journal bearings without cavitation. A change of 24% is observed in dropping of peak pressure values due to cavitation. Initially, this drop is small but later increase with an increase in rotational speed.
2. The oil–vapor distribution in the bearing goes on increasing with the increase in the shaft rotational speeds, thus lowering the value of the pressure build up. The multiphase flow analysis with cavitation hence is extremely important in the case of the bearings operating at higher speeds.
3. The peak pressure increases with an increase in both speed as well as eccentricity ratio, but more sensitive to eccentricity ratio change, thus making the situation tightly coupled. The pressure distribution is wider at lower eccentricity ratio values due to insufficient development of hydrodynamic forces to support the external load, but becomes narrower with an increase in the eccentricity ratio in the range 0.8–0.9 due to suf-
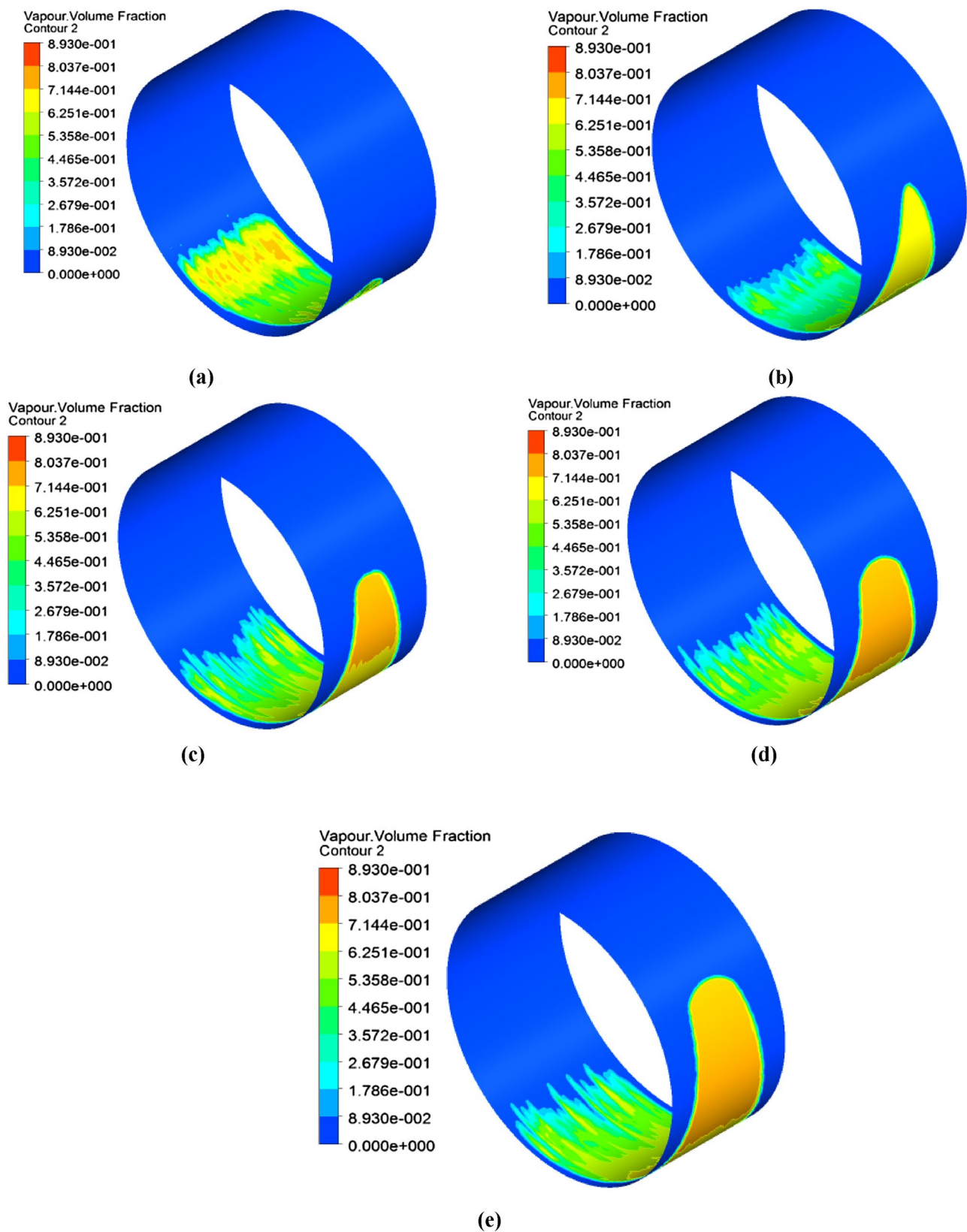
Fig. 17 Vapor volume fraction of oil vapor (%) in the journal bearing for $\varepsilon = 0.8$. **a** 1000 RPM. **b** 2000 RPM. **c** 3000 RPM. **d** 4000 RPM. **e** 5000 RPM

ficient positive pressure values. This justifies the use of hydrodynamic bearings operating at higher eccentricity ratios at speeds.

4. Fluid–structure interaction lowers the values of peak pressure due to bearing shell deformations causing the modification of fluid domain. A reduction of 13% in the peak pressure value is observed.

5. The bearing deformations increase with speed as hydrodynamic pressure forces increase and become significant at higher speed, thereby need to consider for prediction of accurate performance of the bearing.

6. The design optimization approach validated here provides the platform for accurate performance of the bearings by considering the realistic flow conditions as well as deformations in the bearing due to hydrodynamic forces developed in the bearing.

7. The computation time is also significantly reduced by this approach.

Compliance with ethical standards

References

1. Brizmer V, Kligerman Y, Etsion I (2003) A laser surface textured parallel thrust bearing. Tribol Trans 46:397–403. doi:10.1080/05698190490426007

2. Buscaglia GC, Ciuperca I, Jai M (2005) The effect of periodic textures on the static characteristics of thrust bearings. J Tribol 127:899. doi:10.1115/1.2033896

3. D'Agostino V, Senatore A (2006) Analytical solution for two-dimensional Reynolds equation for porous journal bearings. Ind Lubr Tribol 58:110–117. doi:10.1108/00368790610651521

4. Arghir M, Roucou N, Helene M, Frene J (2003) Theoretical analysis of the incompressible laminar flow in a macro-roughness cell. J Tribol 125:309. doi:10.1115/1.1506328

5. Sahlin F, Glavatskih SB, Almqvist T, Larsson R (2005) Two-dimensional CFD-analysis of micro-patterned surfaces in hydrodynamic lubrication. J Tribol ASME 127:96–102. doi:10.1115/1.1828067

6. Li J, Chen H (2007) Evaluation of applicability of Reynolds equation for squared transverse roughness compared to CFD. J Tribol 129:963. doi:10.1115/1.2768619

7. Wodtke M, Olszewski A, Wasilczuk M (2013) Application of the fluid-structure interaction technique for the analysis of hydrodynamic lubrication problems. Proc Inst Mech Eng Part J J Eng Tribol 227:888–897. doi:10.1177/1350650113481147

8. Lin Q, Wei Z, Wang N, Chen W (2013) Analysis of the lubrication performances of the journal bearing system using computational fluid dynamics and fluid-structure interaction considering the thermal influence and cavitation. Tribol Int 64:8–15. doi:10.1016/j.triboint.2013.03.001

9. Gandjalikhan Nassab SA, Maneshian B (2007) Thermohydrodynamic analysis of cavitating journal bearings using three different cavitation models. Proc Inst Mech Eng Part J J Eng Tribol 221:501–514. doi:10.1243/13506501JET238

10. Guo Z, Hirano T, Kirk RG (2005) Application of CFD analysis for rotating machinery—part I: hydrodynamic, hydrostatic bearings, and squeeze film damper. J Eng Gas Turbines Power 127:445. doi:10.1115/1.1807415

11. Chen PYP, Hahn EJ (1998) Use of computational fluid dynamics in hydrodynamic lubrication. Proc Inst Mech Eng Part J J Eng Tribol 212:427–436. doi:10.1243/1350650981542236

12. Tucker PG, Keogh PS (1995) A generalized computational fluid dynamics approach for journal bearing performance prediction. Proc Inst Mech Eng Part J J Eng Tribol 209:99–108. doi:10.1243/PIME_PROC_1995_209_412_02

13. Gertzos KP, Nikolakopoulos PG, Papadopoulos CA (2008) CFD analysis of journal bearing hydrodynamic lubrication by Bingham lubricant. Tribol Int 41:1190–1204. doi:10.1016/j.triboint.2008.03.002

14. Manshoor B, Jaat M, Izzuddin Z, Amir K (2013) CFD analysis of thin film lubricated journal bearing. Procedia Eng 68:56–62. doi:10.1016/j.proeng.2013.12.147

15. Ravikovich YA, Ermilov YI, Pugachev AO et al (2014) Prediction of operational characteristics of fluid-film and gas bearings for high-speed turbomachinery using computational fluid dynamics. In: 29th congress international council aeronautical science ICA, pp 1–8

16. Dhande D, Pande DW, Chatarkar V (2013) Analysis of hydrodynamic journal bearing using fluid structure interaction approach 4(8):33

17. Liu H, Xu H, Ellison PJ, Jin Z (2010) Application of computational fluid dynamics and fluid-structure interaction method to the lubrication study of a rotor-bearing system. Tribol Lett 38:325–336. doi:10.1007/s11249-010-9612-6

18. Lin Qiyin, Zhengying Wei NW (2015) Optimum design of recess parameters for a high-speed hybrid journal bearing using fluid-structure interaction and improved orthogonal experiment method. J Balk Tribol Assoc 21:300–313

19. Lihua Lu, Chen W, Wu B et al (2016) Optimal design of an aerostatic spindle based on fluid-structure interaction method and its verification. Proc Inst Mech Eng Part J J Eng Tribol 230:690–696. doi:10.1177/1350650115611156

20. Geller M, Schemmann C, Kluck N (2014) Simulation of radial journal bearings using the FSI approach and a multi-phase model with integrated cavitation. Prog Comput Fluid Dyn 14:14–23. doi:10.1504/PCFD.2014.059196

21. Riedel M, Schmidt M, Stücke P (2013) Numerical investigation of cavitation flow in a journal bearing geometry. EPJ Web Conf 45:01081. doi:10.1051/epjconf/20134501081

22. Osman TA (2004) Effect of lubricant non-Newtonian behavior and elastic deformation on the dynamic performance of finite journal plastic bearings. Tribol Lett 17:31–40. doi:10.1023/B:TRIL.0000017416.95176.30

23. Montazeri H (2008) Numerical analysis of hydrodynamic journal bearings lubricated with ferrofluid. Proc Inst Mech Eng Part J J Eng Tribol 222:51–60. doi:10.1243/13506501jet314

24. Braun MJ, Hannon WM (2010) Cavitation formation and modeling for fluid film bearings: a review. Proc Inst Mech Eng Part J J Eng Tribol 224:839–863. doi:10.1234/13506501JET772

25. Zwart P, Gerber A, Belamri T (2004) A two-phase flow model for predicting cavitation dynamics. Fifth international conference multiphase flow, Yokohama, Japan, May 30–June 3

26. Cheqamahi JM, Nili-Ahmadabadi M, Akbarzadeh S, Saghafian M (2016) Numerical analysis of turbocharger's bearing using dynamic mesh. J Appl Fluid Mech 9(5):2545–2557